

### IDENTIFICATION OF ANISOTROPIC CONSTITUTIVE MODELS FOR COMPLEX LOADING PATHS

# Multi-interpolation Method to Linearize Stress Path in Cruciform Specimen for In-Plane Biaxial Test

JINJAE KIM,  $^1$  JORDAN HOFFMAN,  $^1$  DILIP K. BANERJEE,  $^2$  MARK A. IADICOLA,  $^2$  BRAD L. KINSEY,  $^1$  and JINJIN HA  $^{\rm D}{}^{\rm 1,3}$ 

1.—Mechanical Engineering, University of New Hampshire, Durham, NH 03824, USA. 2.—Materials Science and Engineering Division, National Institute of Standards and 20899-8553, Technology (NIST), 100 Dr, Gaithersburg, MD Bureau 3.—e-mail: jinjin.ha@unh.edu

A multi-interpolation method is proposed to determine the displacement trajectory along each axis of a cruciform specimen with the goal of achieving a linear stress path, corresponding to a constant stress triaxiality, in the center of the custom-designed, non-standard specimen during in-plane biaxial testing. Finite element simulations are used to obtain the stress path from the given displacement trajectory, which is the displacement histories imposed on the specimen loading arms. In every iteration, the displacement trajectory is updated using the interpolation between the target stress path and adjacent ones on each side of the curve. The iterations are repeated until a linearity tolerance is satisfied. In this study, the material is an austenitic stainless steel, SS316L, with the Hockett-Sherby isotropic hardening model and Yld2004-18p non-quadratic anisotropic yield function. The method is demonstrated for five stress states between pure shear and equibiaxial tension. The results show the successful determination of a displacement trajectory for the non-standard cruciform specimen so that a linear stress path and constant triaxiality at the area of interest are achieved.

#### INTRODUCTION

Sheet metal forming is widely used in manufacturing, e.g., in the automotive, aerospace, and biomedical industries, due to the efficiency for mass production with consistent part quality. Common processes used in these industries include deep drawing, spinning, and roll forming.3 However, the process design and parameter optimization are often time consuming, and require iterative effort if they are solely based on trial-and-error experimentation. In order to overcome this problem, finite element (FE) simulations are utilized to virtually evaluate the process. Key to the prediction accuracy of FE simulations is correct model inputs, such as geometry, boundary conditions, and constitutive models capturing the material behavior during deformation.4-

Selection of constitutive models depends on the materials used in the process, analysis focus of the FE simulation, and level of prediction accuracy required. For example, the von Mises isotropic yield function<sup>8</sup> is often used with an isotropic strain-hardening model<sup>9–12</sup> due to simplicity, but it cannot capture plastic anisotropy and non-linear loading effects, which are important in sheet metal forming. Thus, various yield functions have been vigorously developed in the past decades to better capture the material behavior as experimentally observed, e.g., Barlat, 13-15 Banabic–Balan–Comsa, 16 Plunkett-Barlat, <sup>17</sup> Yoon, <sup>18</sup> etc. Additional complexity, which can be incorporated into modeling efforts, is plastic behavior influenced by deformation-induced microstructural changes. Fahr<sup>19</sup> found that the ductility and strength of austenitic stainless steel can be enhanced through a deformation-induced phase transformation from austenite to martensite phases. Olson and Cohen<sup>20</sup> developed a martensite phase transformation kinetics model, which is a function of equivalent plastic strain. This

(Received June 27, 2023; accepted September 18, 2023)

Published online: 10 October 2023

model was further extended through extensive studies to understand the effects of various factors, such as stress state, <sup>21</sup> strain rate, <sup>22</sup> temperature, <sup>23</sup> etc. In the same vein, Beese and Mohr<sup>24</sup> also proposed a transformation kinetics model with respect to stress states, i.e., stress triaxiality and Lode angle parameter, based on the extensive experimental results available, including uniaxial tension/compression, simple shear, plane strain tension, and equibiaxial tension, which were performed using different types of specimens and machines.

Alternatively, in-plane biaxial testing using a cruciform specimen has been widely used for sheet metals to evaluate the material behavior under numerous stress states, such as uniaxial or biaxial tension, 25-28 pure shear, 29 and biaxial compression. 30,31 The advantage of this testing method is that the same specimen and machine can be used to impose different stress states by simply changing the loading ratios of each arm. However, the standard geometry of a cruciform specimen<sup>26,32</sup> is only able to achieve a small plastic strain, typically < 0.05 to 0.08. 25,26,33–36 This test method is limited by early failure in the arms before the deformation is depleted in the center of the specimen. Geometry modifications to the standard specimen, e.g., a thickness reduction to concentrate the deformation at the desired central locations, <sup>37–42</sup> corner notches to prevent localization, <sup>34,43,44</sup> and cut-outs to remove the unnecessary deformation, 45–48 have been explored. However, inhomogeneities of the deformation fields exist in the gauge section due to locally varied stress states. Mamros et al.<sup>39</sup> confirmed that complicated stress and strain states were observed in their non-standard specimen designed with a thickness reduction and corner notches. The lost homogeneity in the gauge area does not allow traditional measurement of stress using the force signal from the machine divided by the instantaneous crosssectional area. Alternatively, advanced experimental techniques, e.g., in situ x-ray and neutron diffraction, enable the measurement of local stresses<sup>49,50</sup> which are intergranular stresses calculated by crystal lattice strains. However, the loading must be paused during the measurement, which allows some relaxation in the material.

Another issue with employing a non-standard cruciform specimen geometry is the difficulty in obtaining a linear stress path when simple boundary conditions, e.g., a linear force or displacement trajectory applied to the arms, are used. This creates non-linear stress paths that interrupt the measurement due to the loading history dependency of plasticity and martensite transformation kinetics, and makes it difficult to characterize material behavior under a specific stress state, e.g., uniaxial tension, shear, equibiaxial tension, etc., equivalent

to a constant stress triaxiality or Lode angle parameter. <sup>24</sup> Hoffman et al. <sup>51</sup> presented a double interpolation method to achieve a non-linear displacement trajectory producing a linear strain path, but the corresponding stress path was still non-linear. Therefore, a new methodology is needed to achieve a non-linear displacement trajectory corresponding to a linear stress path. It should be noted that some, but not all, cruciform test machines utilize closed loop control to follow a desired strain or stress deformation path. <sup>52–54</sup>

This study is an extension of the previous work<sup>51</sup> focusing on determining a linear stress, instead of strain, path that is necessary to characterize martensite transformation kinetics in austenitic stainless steels. A multi-interpolation method using FE simulations is proposed to determine the nonlinear displacement trajectories needed to achieve the desired linear stress paths using a non-standard cruciform specimen. Five target stress paths will be considered between pure shear and equibiaxial tension. The Hockett–Sherby isotropic strain-hard-ening model<sup>11</sup> and Yld20004-18p non-quadratic anisotropic plasticity yield function<sup>14</sup> are used to describe the material behavior of SS316L. The following sections will describe the non-standard cruciform specimen geometry used, present the material models implemented, explain the multiinterpolation method utilized, provide details related to the numerical simulations, and show the results for SS316L.

# NON-STANDARD CRUCIFORM SPECIMEN GEOMETRY

The non-standard cruciform specimen geometry used in this work is taken from a paper by Mamros et al.<sup>39</sup> They optimized a specimen of austenitic stainless steel SS316L with corner notches and a central pocket to achieve higher strain than the standard specimen.<sup>26,32</sup> A schematic of the specimen geometry is shown in Fig. 1, and the dimensions are summarized in Table I.

# MATERIAL MODELING FOR ANISOTROPIC PLASTICITY

Since this study utilizes a non-standard cruciform specimen optimized for SS316L,  $^{39}$  the same material model and parameters from the reference are used here. Hooke's law for isotropic linear elasticity is assumed with a Young's modulus  $E=193.8~\mathrm{GPa}$  and Poisson's ratio v=0.33. The equivalent stressstrain relationship  $(\overline{\sigma}-\overline{\epsilon})$  of SS316L is described by the Hockett–Sherby isotropic strain-hardening model:  $^{11}$ 

$$\overline{\sigma} = H - (H - \sigma_0) \cdot \exp(-Q \cdot \overline{\varepsilon}^n)$$
 (1)

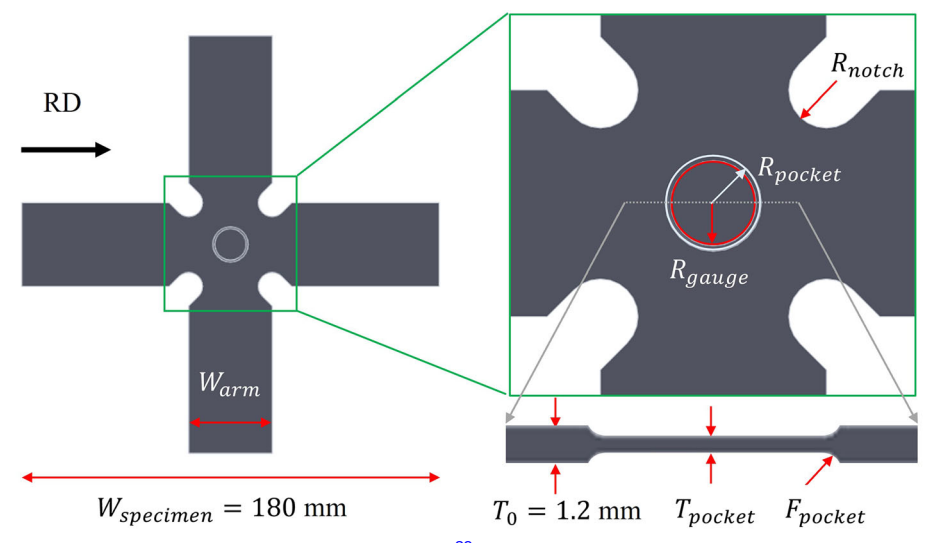


Fig. 1. Schematic of the non-standard cruciform specimen geometry.<sup>39</sup>

# Table I. Dimensions of the non-standard cruciform specimen<sup>39</sup>

Radius of pocket flat area $(R_{\text{gauge}})$	5.65 mm
Fillet radius of pocket $(F_{pocket})$ Arm width $(W_{arm})$	1.5 mm 30 mm
Initial thickness $(T_0)$	1.2 mm
Thickness of pocket $(T_{pocket})$	0.6 mm
Corner notch radius $(\vec{R}_{\text{notch}})$	5 mm

Table II. Material parameters of the Hockett-Sherby isotropic strain-hardening model<sup>39</sup>

$\sigma_0$ (MPa)	H (MPa)	Q	n
339.48	1445.44	1.81	0.89

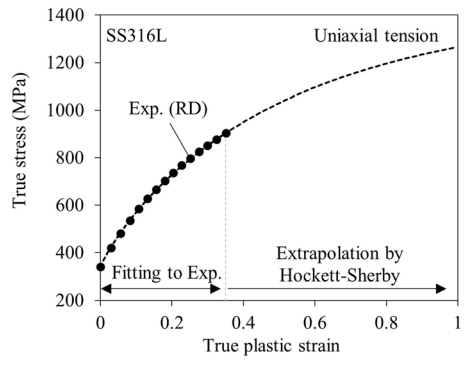


Fig. 2. Stress-strain curve from uniaxial tension experiment in the RD and the Hockett-Sherby isotropic strain-hardening model.<sup>39</sup>

where  $\sigma_0$  is the initial yield stress and H, Q, and n are material parameters (Table II), which are identified by fitting the stress–strain curve obtained from the uniaxial tensile test in the rolling direction (RD) (Fig. 2).

In addition to the strain-hardening behavior, the plastic anisotropy of SS316L and its evolution with plastic work are captured by the Yld2004-18p non-quadratic anisotropic plasticity yield function. The model is formulated with six stress components, i.e.,  $\sigma_{ij(i,j=1-3)}$ :  $\sigma_{11}$ ,  $\sigma_{22}$ ,  $\sigma_{33}$ ,  $\sigma_{12} = \sigma_{21}$ ,  $\sigma_{13} = \sigma_{31}$ , and  $\sigma_{23} = \sigma_{32}$ , which are applicable for a solid element FE model, as follows:

$$\phi = \phi(\tilde{\mathbf{S}}', \tilde{\mathbf{S}}'') = \left| \tilde{S}_{1}' - \tilde{S}_{1}'' \right|^{a} + \left| \tilde{S}_{1}' - \tilde{S}_{2}'' \right|^{a} + \left| \tilde{S}_{1}' - \tilde{S}_{3}'' \right|^{a} + \left| \tilde{S}_{2}' - \tilde{S}_{3}'' \right|^{a} + \left| \tilde{S}_{2}' - \tilde{S}_{3}'' \right|^{a} + \left| \tilde{S}_{3}' - \tilde{S}_$$

where a is the exponent, suggested as a=8 for face-centered cubic crystal structures.  $\tilde{\boldsymbol{S}}'$  and  $\tilde{\boldsymbol{S}}''$  are linearly transformed deviatoric stress tensors, and  $\tilde{S}'_{j(j=1-3)}$  are their principal stresses. The linear transformations of the stress tensor are achieved with the transformation matrices,  $\tilde{\boldsymbol{C}}'$  and  $\tilde{\boldsymbol{C}}''$ , as:

$$\tilde{\mathbf{S}}' = \tilde{\mathbf{C}}' \cdot \mathbf{S} 
\tilde{\mathbf{S}}'' = \tilde{\mathbf{C}}'' \cdot \mathbf{S}$$
(3)

which include 18 anisotropic parameters, i.e.,  $\alpha_{k(k=1-18)}$ . The detailed description of the Yld2004-18p yield function and the tensor transformation with anisotropic parameters can be found in Ref. 14 The plastic anisotropy evolution of SS316L, experimentally observed in Ref. 39 is captured by formulating the anisotropic parameters as a function of equivalent plastic strain  $\bar{\epsilon}$ :

$$\alpha_{\mathbf{k}(\mathbf{k}=1-18)}(\overline{\varepsilon}) = A_{\mathbf{k}} - B_{\mathbf{k}} \cdot \exp(-D_{\mathbf{k}} \cdot \overline{\varepsilon})$$
 (4)

Table III. Anisotropic	parameters	of	Yld2004-18p
vield function <sup>39</sup>	_		_

$\alpha_{\mathbf{k}}$	$A_{\mathbf{k}}$	$B_{\mathrm{k}}$	$D_{\mathbf{k}}$
1	0.93	-0.06	10
2	0.56	-0.10	27
3	0.71	0.06	45
4	0.80	-0.13	25
5	0.88	-0.03	35
6	0.89	0.01	8
7	1.22	-0.01	30
8	1.23	-0.03	5
9	0.99	0.18	20
10	1.40	0.12	4
11	1.40	-0.03	3
12	1.22	0.21	17
13	1.25	0.07	20
14	1.12	0.03	20
15	1.11	-0.03	27
16	0.89	-0.02	3
17	0.88	-0.01	20
18	1.20	-0.10	30

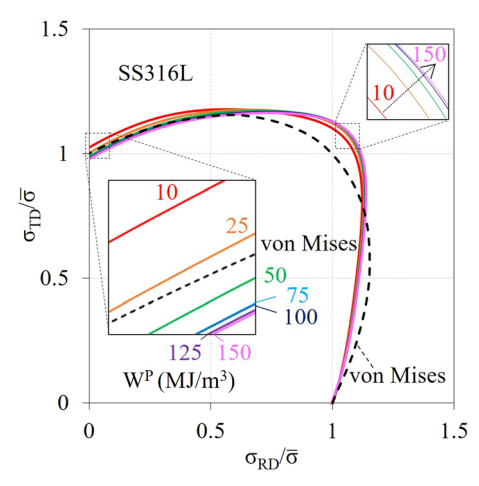


Fig. 3. Evolution of Yld2004-18p yield loci at 7 plastic work levels: contracting uniaxial and plane strain tensions (TD) and expanding outward near equibiaxial tension stress states according to increment of plastic work.<sup>39</sup>

where  $A_{\rm k},\,B_{\rm k}$ , and  $D_{\rm k}$  are constants for each  $\alpha_{\rm k}$ , as summarized in Table III. The corresponding yield loci evolution is visualized in Fig. 3 for 7 plastic work levels from 10 MJ/m³ to 150 MJ/m³. As is shown, the shape of the yield loci contracts during plastic deformation near the uniaxial and plane strain tensions in the transverse direction (TD) and expands outward near the equibiaxial tension stress state.

# MULTI-INTERPOLATION METHOD

In this work, a multi-interpolation method is used to determine a displacement trajectory for the arms of the cruciform specimen to achieve a linear stress path, which is equivalent to deformation under a constant stress triaxiality, in the center pocket area. This is an extension of the interpolation method used in Ref. 51 which considered strain, as opposed to stress, trajectories and only performed two iterations of the interpolation. For each interpolation step, a new displacement trajectory is obtained by interpolating two reference displacement trajectories using weighting factors, which are calculated by the interpolation of two reference stress paths (Ref. 1 and Ref. 2 in Fig. 4) to the target stress path. Since the target is the result of interpolation using two references and weighting factors, the two references must be located on opposite sides of the target path. Thus, two references are the minimum number required, and more than two are necessary if the target path and the references cross over each other. Note that the simplest case of interpolation method (with two reference paths) is first explained in the current section. However, the actual application to the cruciform simulation is much more complicated (with more than two reference paths), and thus the interpolation procedure will be explained again step-by-step for pure shear condition in Section "Results and Discussion". Figure 4a and b describes the details of the interpolation method at a specific point in the stress path and displacement trajectory, respectively. It should be noted that the 11-direction is the RD, and also the major loading direction, which is located along the y-axis.

First, the initial reference stress paths (Ref. 1 and Ref. 2) in Fig. 4a are obtained from FE simulations with linear displacement trajectories near the target defined by the slope m of the target stress path. Then, for each time step of the FE simulation results, the interpolation point  $(\sigma_{22}, \sigma_{11})_*$  on the target path is found by an intersection between  $(\sigma_{22}, \sigma_{11})_1$  and  $(\sigma_{22}, \sigma_{11})_2$  on the Ref. 1 and Ref. 2 paths, respectively. By this definition, the interpolation point of the minor loading direction on the target,  $(\sigma_{22})_*$ , can be found as:

$$(\sigma_{22})_* = \frac{\left| (\sigma_{11})_2 - \left| \frac{(\sigma_{11})_2 - (\sigma_{11})_1}{(\sigma_{22})_2 - (\sigma_{22})_1} \right| \times (\sigma_{22})_2 \right|}{\left( m - \left| \frac{(\sigma_{11})_2 - (\sigma_{11})_1}{(\sigma_{22})_2 - (\sigma_{22})_1} \right| \right)}$$
(5)

Once  $(\sigma_{22})_*$  is obtained from Eq. 5,  $(\sigma_{11})_*$  is calculated using the linear relationship with the slope m, i.e.,  $(\sigma_{11})_* = m \cdot (\sigma_{22})_*$ , the weighting factors a' and b', which represent the interpolating ratio between the two references onto the target path, can be determined from:

$$a' = \sqrt{\left\{ (\sigma_{22})_* - (\sigma_{22})_1 \right\}^2 + \left\{ (\sigma_{11})_* - (\sigma_{11})_1 \right\}^2}$$

$$b' = \sqrt{\left\{ (\sigma_{22})_2 - (\sigma_{22})_* \right\}^2 + \left\{ (\sigma_{11})_2 - (\sigma_{11})_* \right\}^2}$$
(6)

Then, the new displacement trajectory can be calculated using the same interpolation method and the weighting factors between two reference displacement trajectories:

Multi-interpolation Method to Linearize Stress Path in Cruciform Specimen for In-Plane Biaxial Test

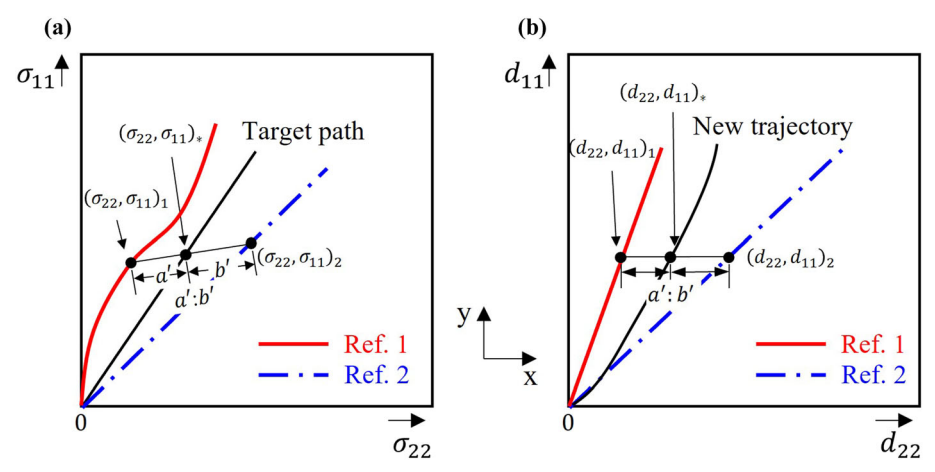


Fig. 4. Schematic of the interpolation method: (a) determination of weighting factors a' and b' interpolating two reference stress paths (Ref. 1 and Ref. 2, red dash and blue dash-dot lines, respectively) to a target path (solid black line), and (b) new displacement trajectory determined by interpolation of two references (Ref. 1 and Ref. 2) using the same weighting factors (Color figure online).

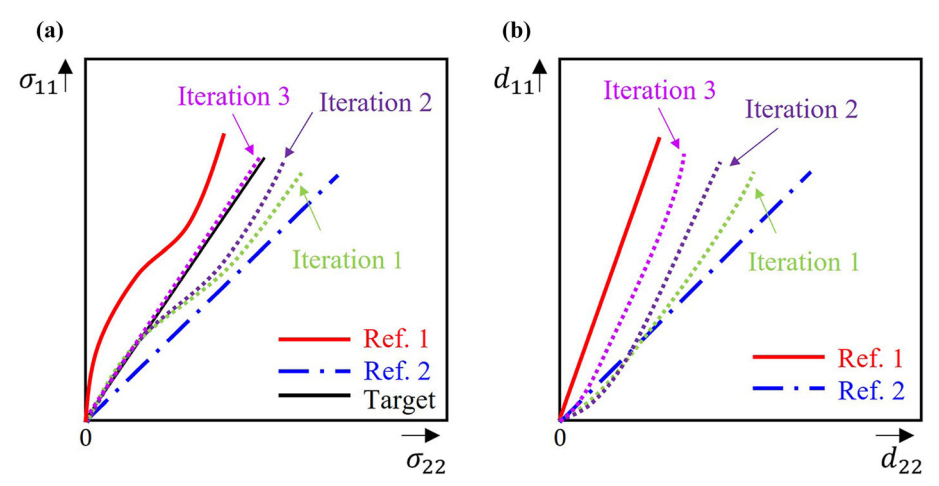


Fig. 5. Schematic of iterative progression for multi-interpolation method: (a) successive iterations of the stress interpolation approaching the target linear path, and (b) displacement trajectories shifting with iterations.

$$(d_{22})_* = (d_{22})_1 + \frac{a'}{a' + b'} \cdot L$$
 (7)

where  $L=(d_{22})_2-(d_{22})_1$  is the distance in the 22-direction of the two points obtained at the same time step on the two references (Fig. 4b). Note that the displacement increment in the 11-direction at each time step is controlled by the boundary condition in the simulations as the same value for the two references, i.e.,  $(d_{11})_1=(d_{11})_2=(d_{11})_*$ . The entire displacement trajectory is obtained through the same procedure at each time step of FE simulation. Note that the same weighting factors are used for both stress path and displacement trajectory, even though they are not linearly related.

To achieve the optimized displacement trajectory producing the linear stress path that agrees with the target stress ratio m, the displacement trajectory is continuously updated through multiple iterations. For each iteration, one of the references is

replaced by the displacement trajectory determined in the last iteration so that the new references are closer to the target. The procedure for the multi-interpolation method is described schematically in Fig. 5. Figure 5a depicts the progression of nonlinear stress paths toward the linear target through the iterations, while Fig. 5b illustrates the corresponding non-linear displacement trajectories.

Multi-interpolations are performed until the predefined tolerance condition is satisfied. In this study, two termination criteria are used. One is to evaluate the total error of the stress path from the target, i.e., sum of square error (SSE), which is calculated with respect to the stress triaxiality. Each target with a specific slope m is selected to have a unique stress triaxiality value. The SSE is expressed by:

$$SSE = \sum_{n=1}^{\text{tot}} (\eta_n - \eta^t)^2$$
 (8)

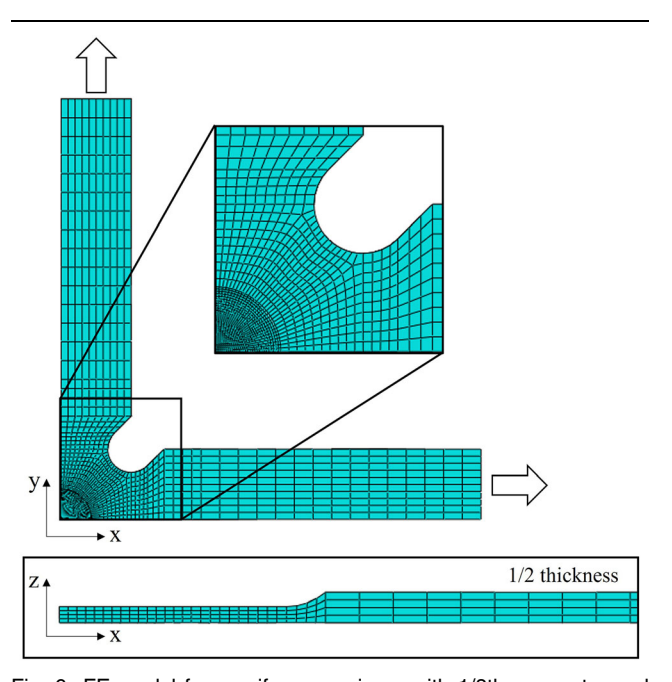
where tot is total number of time steps.  $\eta_n$  is the stress triaxiality calculated by the mean hydrostatic pressure  $(\sigma_m)$  and equivalent stress  $(\overline{\sigma})$ , i.e.,  $\eta_n = (\sigma_m/\overline{\sigma})_n$ , and  $\eta^t$  is the target stress triaxiality. In addition, one more termination criterion,  $\Delta SSE$  based on the difference in consecutive SSE at the previous (n-1)th and current (n)th iterations, is considered to assure optimization robustness of multi-interpolation method:

$$\Delta SSE = |SSE_n - SSE_{n-1}| \tag{9}$$

In this study, the tolerance conditions used to terminate the interpolation progression are SSE  $\leq$  0.13 and  $\Delta$ SSE  $\leq$  0.03, which are determined based on the data. These criteria ensure balancing between the accuracy of interpolation method and the robustness of the iteration procedure when performing multi-interpolations.

### FINITE ELEMENT ANALYSIS

The material models discussed previously, i.e., Hooke's linear elasticity and Yld2004-18p non-quadratic anisotropic plasticity yield function combined with the Hockett-Sherby isotropic strain-hardening model, are implemented into a user-defined material subroutine (UMAT) for ABAQUS/Standard 2022. In order to reduce the computational time, a 1/8th geometry of the cruciform specimen is modeled by considering the orthotropic symmetry in the material orientation and the specimen geometry. The specimen is meshed with 8-node linear brick elements with reduced integration (C3D8R), as shown in Fig. 6. Finer meshes are assigned in the center pocket area while the meshes along the arms are coarser. Four elements are



included through the half-thickness. A displacement boundary condition is applied at the end of each arm, where the specimen is gripped in the experiment.

Figure 7a and b shows the linear displacement trajectories  $\left(d_{d_{22}:d_{11}}^L\right)$  applied to the end of arms and the corresponding stress paths  $\left(\sigma_{d_{22}:d_{11}}^0\right)$ , respectively. tively. (Please refer to the nomenclature in Appendix A). It should be noted that the stress paths are extracted from the surface element for a central integration point located at the center of the pocket, assuming the deformation within a 1 mm radius from the center is uniform in a practical sense. This range is chosen because the area is large enough for x-ray or neutron diffraction measurements. Target stress paths  $\left(\sigma_{\sigma_{22}:\sigma_{11}}^{t}\right)$  are selected, specifically  $\sigma_{-1:1}^{t}$  (near pure shear),  $\sigma_{-1:2}^{t}$ ,  $\sigma_{0:1}^{t}$  (uniaxial tension),  $\sigma_{1:2}^{t}$  (near plane strain tension), and  $\sigma_{1:1}^{t}$  (equibiaxial tension), which are equivalent to  $\eta^{t} = 0$ , 0.111, 0.333, 0.505, and 0.666, respectively. To ensure that there are sufficient references for each target, FE simulations with ten linear displacement trajectories, i.e.,  $d_{-7:6}^L$ ,  $d_{-1:1}^L$ ,  $d_{-2:3}^L$ ,  $d_{-1:2}^L$ ,  $d_{-1:3}^L$ ,  $d_{0:1}^L$ ,  $d_{1:2}^L$ ,  $d_{2:3}^L$ ,  $d_{1:1}^L$ , and  $d_{4:3}^L$  (Fig. 7a), were conducted, and the corresponding ten stress paths, i.e.,  $\sigma_{-7:6}^0$ ,  $\sigma_{-1:1}^0$ ,  $\sigma_{-2:3}^0$ ,  $\sigma_{-1:2}^0$ ,  $\sigma_{0:1}^0$ ,  $\sigma_{0:1}^0$ ,  $\sigma_{1:2}^0$ ,  $\sigma_{0:3}^0$ ,  $\sigma_{1:1}^0$ , and  $\sigma_{4:3}^0$  (Fig. 7b), were obtained as references. The stress paths are specifically as the stress paths are significant to the stress paths. generated by linear displacements are highly nonlinear (Fig. 7b), except for  $\sigma_{1.1}^0$ .

# RESULTS AND DISCUSSION

The multi-interpolation process has been applied to each stress path individually. Figure 8 shows an example of the multi-interpolation procedure for pure shear, i.e.,  $\sigma_{-1\cdot 1}^t$ , equivalent to  $\eta_{-1\cdot 1}^t=0$ . (Please refer to the nomenclature in Appendix A). In the first iteration, the interpolation is performed in three segments due to intersections, i.e., when  $\sigma_{11}$  < 447 MPa, 447 MPa  $\leq \sigma_{11}$  < 643 MPa, and  $643 \text{ MPa} \leq \sigma_{11}$  , with different sets of reference stress paths among  $\sigma_{-7:6}^0$ ,  $\sigma_{-1:1}^0$ ,  $\sigma_{-2:3}^0$ , and  $\sigma_{-1:2}^0$ . For the first segment, when  $\sigma_{11} < 447$  MPa,  $\sigma_{-7:6}^0$  and  $\sigma_{-1:1}^0$  are used as the two references because they are located on opposite sides of the target path and are the closest ones before  $\sigma_{-1:1}^0$  crosses over the target. Then,  $\sigma_{-1:1}^0$  and  $\sigma_{-2:3}^0$  are the new references for the second segment when 447 MPa  $\leq \sigma_{11} < 643$  MPa, and, finally,  $\sigma_{-2:3}^0$  and  $\sigma_{-1:2}^0$  are used for the rest of path when  $643\,\mathrm{MPa} \leq \sigma_{11}^{-1.2}$ . After the first iteration, the new displacement trajectory, i.e.,  $d_{-1:1}^1$ , is determined, as shown in Fig. 8 (black dash lines). The superscript indicates the number of interpolation iterations. Even after this first interpolation, the stress path is significantly closer to the target (Fig. 8a). The corresponding non-linear displacement trajectory (Fig. 8b) is found between the

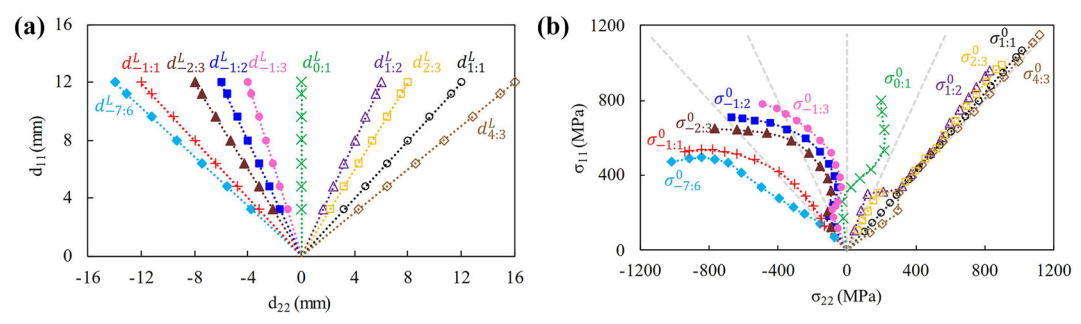


Fig. 7. Initial data used for the multi-interpolation method: (a) ten linear displacement trajectories, and (b) corresponding stress paths and five target paths (gray dash lines) (Color figure online).

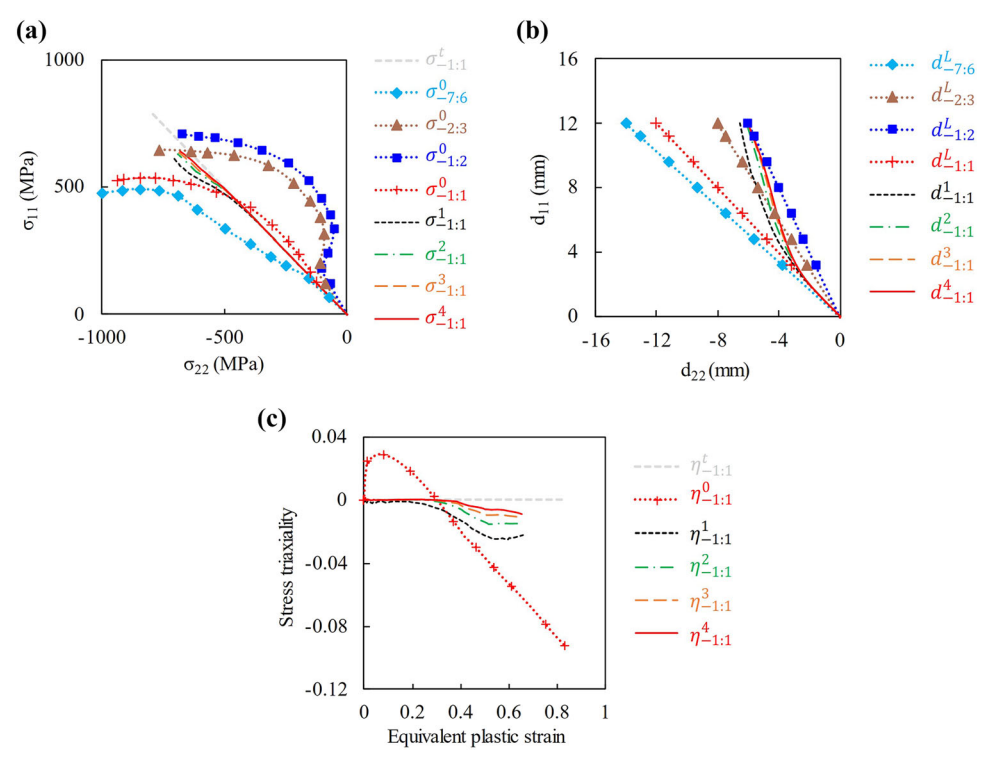


Fig. 8. Progression of multi-interpolation: (a) stress paths  $\sigma_{-1:1}^{i=1,4}$ , corresponding (b) displacement trajectories  $\sigma_{-1:1}^{i=1,4}$ , and (c) stress triaxialities  $\sigma_{-1:1}^{i=1,4}$  (Color figure online).

Table IV. Progression of SSE and  $\Delta SSE$  during multi-interpolation  $\sigma_{-1:1}^{i\,=\,1,4}$ 

Iteration	SSE	$\Delta SSE$	
0	4.096	-	
1	0.275	3.821	
2	0.102	0.173	
3	0.043	0.059	
4	0.021	0.022	

references. From  $\sigma^1_{-1:1}$ , the stress triaxiality  $\eta^1_{-1:1}$  in Fig. 8c is calculated based on the extracted data to evaluate the error. The SSE of the first iteration, obtained from Eq. 8, is 4.096 (Table IV), and thus requires a second iteration, since it is significantly higher than the pre-defined tolerance of SSE  $\leq 0.13$ .

In the second iteration, the references are updated to new ones closer to the target path to narrow down the interpolation range. One of the old references,  $\sigma_{-7:6}^0$ , is replaced by  $\sigma_{-1:1}^1$ , but three others,  $\sigma_{-1:1}^0$ ,  $\sigma_{-2:3}^0$ , and  $\sigma_{-1:2}^0$ , are used again. The second iteration is performed in the same manner as the first one and obtains  $\sigma_{-1:1}^2$  and  $d_{-1:1}^2$ , as shown in Fig. 8a and b (green dash dot lines). The SSE is reduced to 0.102 (< 0.13), but the  $\Delta SSE$  still exceeds the tolerance at 0.173 (> 0.03). Thus, the same procedure is repeated for four iterations until the termination criteria are fully satisfied, i.e., SSE  $\leq$  0.13 and  $\Delta SSE \leq$  0.03. During the consecutive interpolations, the stress path and the triaxiality (Fig. 8c) clearly show the progression to the target path, and become much more linear compared to the first, single interpolation. The corresponding non-

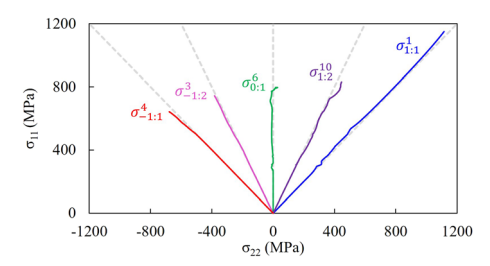


Fig. 9. Linearized stress paths (solid lines) near the target paths (gray dash lines) after multi-interpolation (Color figure online).

linear displacement trajectories, which cross over several linear trajectories, are compared in Fig. 8b. It should also be noted that the average SSE for the central integration point at surface elements located within a 1 mm radius from the center is 0.017, which is nearly 10 times smaller than the termination criteria; thus, the data extraction from the center element is reasonable.

Similarly, the interpolation process is performed for the other four stress paths, i.e.,  $\sigma_{-1:2}^t$ ,  $\sigma_{0:1}^t$ ,  $\sigma_{1:2}^t$ , and  $\sigma_{1:1}^t$ . Each interpolation begins with a set of reference paths and continues until both termination criteria are satisfied (see Appendix B). The results of the multi-interpolation process are shown in Fig. 9 for the linearized stress paths near the targets, and in Fig. 10 for the corresponding nonlinear displacement trajectories. Figure 11 shows the stress triaxiality from the stress paths in Fig. 9. The gray dash lines are the targets for comparison. The superscript indicates the number of interpolation iterations required to satisfy the termination criteria for the target stress path. Based on the results, it can be concluded that the constant stress triaxiality can be successfully achieved by the proposed multi-interpolation method. Moreover, it should be noted that the multi-interpolation method can be applied to any non-standard specimen geometry.

## **CONCLUSION**

A multi-interpolation method has been introduced to determine a non-linear displacement trajectory which can produce a linear stress path, i.e., constant stress triaxiality, in the center reduced thickness pocket area of a non-standard cruciform specimen. FE simulations have been performed using material models, i.e., Hooke's linear elasticity and Yld2004-18p non-quadratic anisotropic plasticity yield function combined with the Hockett-Sherby isotropic strain-hardening model, describe the elasto-plastic deformation behavior of the SS316L material. The interpolation procedure is applied to five target stress paths between pure shear and equibiaxial tension, and iterated to linearize the stress paths near the targets. Initially, two or more reference paths were produced by

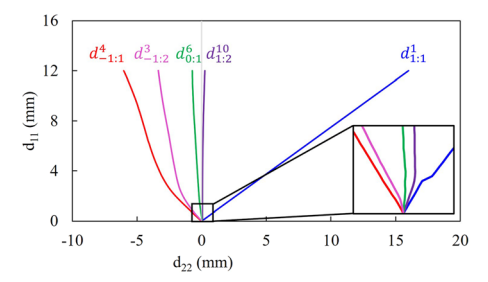


Fig. 10. Displacement trajectories producing the nearly linear stress paths from multi-interpolation.

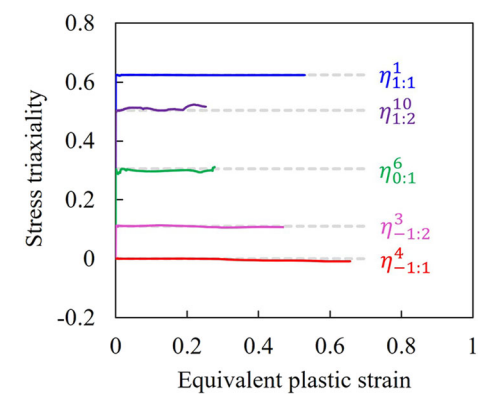


Fig. 11. Stress triaxiality of five nearly linear stress paths (solid lines) and targets (gray dash lines) (Color figure online).

linear displacement trajectories, and replaced by the closest one to the target for each iteration. Two termination criteria were used to achieve accurate results, which were evaluated by SSE(< 0.13), and to ensure robustness of the iteration method with  $\Delta SSE(\leq 0.03)$ . As the number of iterations increases, the stress paths clearly show the progression to the target paths and the corresponding stress triaxialities get closer to constant values. Using these non-linear displacement trajectories, experiments imposing constant stress triaxialities can be conducted to assess, e.g., the austenite to martensite transformation, which is affected by stress state. Future experiments will validate the numerical simulations and this methodology to determine the non-linear displacement trajectories.

### ACKNOWLEDGEMENTS

The authors would like to acknowledge the partial supports from the NH BioMade, US National Science Foundation EPSCoR award (NSF #1757371), and the National Institute of Standards and Technology, through the Summer Undergraduate Research Fellowship (SURF) program for Jordan Hoffmann. We also thank Matthew Eaton and Riley Desmarais for their contributions to the FE simulations.

## **FUNDING**

National Science Foundation (1757371), National Institute of Standards and Technology, Summer Undergraduate Research Fellowship (SURF).

## CONFLICT OF INTEREST

Certain equipment, instruments, software, or materials are identified in this paper in order to specify the experimental procedure adequately. Such identification is not intended to imply recommendation or endorsement of any product or service by NIST, nor is it intended to imply that the materials or equipment identified are necessarily the best available for the purpose.

### APPENDIX A: NOMENCLATURE

Nomenclature used in this study is provided in Table V.

Table V. Summary of nomenclature used in this paper

a' and $b'$	Interpolating ratio between two references (Refs. 1 and 2) and target path
$(\sigma_{22},\sigma_{11})_{1,2,*}$	Interpolation points on Refs. 1 and 2 and target (*) stress paths
$(d_{22},d_{11})_{1,2,st}$	Interpolation points on displacement trajectories corresponding to $(\sigma_{22}, \sigma_{11})_{1,2,*}$
$\sigma_{ m m}$	Mean hydrostatic pressure
$\overline{\sigma}$	Equivalent stress
$\eta_{ m n}$	Stress triaxiality at nth time step of FE
	simulation, i.e., $\eta_{\rm n} = (\sigma_{\rm m}/\overline{\sigma})_{\rm n}$
$d^{L}_{d_{22}:d_{11}}$	Linear displacement trajectory of $d_{22}:d_{11}$
22 11	ratio
$\sigma^0_{d^L_{29}:d^L_{11}}$	Initial stress path produced by linear dis-
$a_{22}^2:a_{11}^2$	placement trajectory $d^L_{d_{22}:d_{11}}$
$\sigma^{ ext{t}}_{\sigma_{22}:\sigma_{11}}$	Target stress path of $\sigma_{22}:\sigma_{11}$ ratio
$\eta^t_{\sigma_{22}:\sigma_{11}}$	Target stress triaxiality corresponding to
$\sigma_{22}:\sigma_{11}$	target stress path $\sigma_{g_2:\sigma_{11}}^{ m t}$
$\sigma^i_{\sigma_{22}:\sigma_{11}}$	Stress path at ith iteration of interpolation
$d^{\mathrm{i}}_{\sigma_{22}:\sigma_{11}}$	Displacement trajectory at ith iteration of
$\sigma_{22}$ : $\sigma_{11}$	interpolation corresponding to $\sigma^{ ext{i}}_{\sigma_{22}:\sigma_{11}}$
i	Stress triaxiality at ith iteration of inter-
$\eta^{ ext{i}}_{\sigma_{22}:\sigma_{11}}$	· · · · · · · · · · · · · · · · · · ·
COL	polation corresponding to $\sigma^1_{d_{22}:d_{11}}$
SSE	Sum of square error
$\Delta SSE$	Difference in consecutive SSE

# APPENDIX B: PROGRESSION OF INTERPOLATION TERMINATION **CRITERIA**

Termination criteria values for each interpolation of the target stress path are provided in Table VI.

Table VI. Termination criteria values for each stress path (with  $\sigma_{-1:1}^{t}$  in Table IV)

Target stress path	Iteration	SSE	ΔSSE
$\sigma_{-1:2}^{ m t}$	0	4.583	_
	1	0.550	4.033
$\left(\eta_{-1:2}^{ m t}\ =\ 0.111 ight)$	2	0.022	0.528
	3	0.012	0.010
$\sigma_{0:1}^{ ext{t}}$	0	13.287	_
	1	1.799	11.488
$\left(\eta_{0:1}^{ m t}\ =\ 0.333 ight)$	2	0.591	1.208
	3	0.213	0.378
	4	0.194	0.019
	5	0.060	0.134
	6	0.049	0.011
$\sigma_{1:2}^{ ext{t}}$	0	11.065	_
	1	8.346	2.719
$\left(\eta_{1:2}^{ m t}\ =\ 0.505 ight)$	2	3.637	4.709
	3	3.211	0.426
	4	1.471	1.740
	5	0.435	1.036
	6	0.708	0.273
	7	1.149	0.441
	8	0.229	0.920
	9	0.102	0.127
	10	0.074	0.028
$\sigma_{1:1}^{ ext{t}}$	0	$1.616\mathrm{E}{-4}$	_
$(\eta_{1:1}^{ m t}=0.666)$	1	1.471E-4	1.444E-05

## REFERENCES

- 1. S.T. Atul and M.C.L. Babu, Proc. Inst. Mech. Eng. B J. Eng. Manuf. 233, 1011 (2019).
- Q. Xia, G. Xiao, H. Long, X. Cheng, and X. Sheng, Int. J. Mach. Tools Manuf. 85, 100 (2014).
- 3. G.T. Halmos, Roll Forming Handbook (CRC Press, Boca Raton, FL, USA, 2005).
  J.J. Kim, Q.T. Pham, and Y.S. Kim, Int. J. Mech. Sci. 191,
- 106067 (2021).
- J. Ha, S. Coppieters, and Y.P. Korkolis, Int. J. Mech. Sci. 182, 105706 (2020).
- J.W. Lee, M.G. Lee, and F. Barlat, Int. J. Plast. 29, 13 (2012).
- M.G. Lee, D. Kim, C. Kim, M.L. Wenner, and K. Chung, Int. J. Plast. 21, 915 (2005).
- R.V. Mises, Nachr. Ges. Wiss. Zu Gött. Math. Phys. Kl. 1913, 582 (1913).
- 9. E. Voce, J. Inst. Met. 74, 537 (1948).
- 10. H.W. Swift, J. Mech. Phys. Solids 1, 1 (1952).
- 11. J.E. Hockett and O.D. Sherby, J. Mech. Phys. Solids 23, 87 (1975).
- Q.T. Pham, B.H. Lee, K.C. Park, and Y.S. Kim, Int. J. Mech. Sci. 140, 521 (2018).
- F. Barlat and K. Lian, Int. J. Plast. 5, 51 (1989).
- F. Barlat, H. Aretz, J.W. Yoon, M.E. Karabin, J.C. Brem, and R.E. Dick, Int. J. Plast. 21, 1009 (2005).

- F. Barlat, J.C. Brem, J.W. Yoon, K. Chung, R.E. Dick, D.J. Lege, F. Pourboghrat, S.H. Choi, and E. Chu, *Int. J. Plast.* 19, 1297 (2003).
- D. Banabic, H. Aretz, D.S. Comsa, and L. Paraianu, Int. J. Plast. 21, 493 (2005).
- O. Cazacu, B. Plunkett, and F. Barlat, Int. J. Plast. 22, 1171 (2006).
- J.W. Yoon, Y. Lou, J. Yoon, and M.V. Glazoff, Int. J. Plast. 56, 184 (2014).
- 19. D. Fahr, Metall. Trans. 2, 1883 (1971).
- 20. G.B. Olson and M. Cohen, Metall. Trans. A 6, 791 (1975).
- Z. Feng, M. Zecevic, and M. Knezevic, Int. J. Plast. 136, 102807 (2021).
- Z. Feng, R. Pokharel, S.C. Vogel, R.A. Lebensohn, D. Pagan, E. Zepeda-Alarcon, B. Clausen, R. Martinez, G.T. Gray, and M. Knezevic, *Int. J. Plast.* 156, 103367 (2022).
- M. Zecevic, M.V. Upadhyay, E. Polatidis, T. Panzner, H. Van Swygenhoven, and M. Knezevic, Acta Mater. 166, 386 (2019)
- 24. A.M. Beese and D. Mohr, Acta Mater. 59, 2589 (2011).
- M. Ishiki, T. Kuwabara, and Y. Hayashida, *Int.J. Mater. Form.* 4, 193 (2011).
- T. Kuwabara, S. Ikeda, and K. Kuroda, J. Mater. Process. Technol. 80–81, 517 (1998).
- T. Kuwabara, T. Mori, M. Asano, T. Hakoyama, and F. Barlat, *Int. J. Plast.* 93, 164 (2017).
- N. Deng, T. Kuwabara, and Y.P. Korkolis, Int. J. Mech. Sci. 138–139, 383 (2018).
- X. Kong, L. Helfen, M. Hurst, D. Hänschke, D. Missoum-Benziane, J. Besson, T. Baumbach, and T.F. Morgeneyer, Acta Mater. 231, 117842 (2022).
- M.C. Serna Moreno, and S. Horta Muñoz, Compos. Struct. 234, 111697 (2020).
- V. Giannella, D. Amato, and M. Perrella, Eng. Fract. Mech. 261, 108247 (2022).
- 32. ISO, 16842:2021 1 (2021).
- Y. Hanabusa, H. Takizawa, and T. Kuwabara, J. Mater. Process. Technol. 213, 961 (2013).
- 34. M.A. Iadicola, A.A. Creuziger, and T. Foecke, Advanced biaxial cruciform testing at the NIST center for automotive lightweighting. Paper Presented at the Society for Experimental Mechanics, Lombard, IL, USA, 3–6 June 2014.
- Y.P. Korkolis, N. Deng, and T. Kuwabara, Biaxial unloading and springback behavior of dual-phase DP590 steel using cruciform specimens. Paper presented at the NUMISHEET 2014: The 9th International Conference and Workshop on Numerical Simulation of 3D Sheet Metal Forming Processes Melbourne, Australia, 6–10 Jan 2014.
- Y. Hanabusa, H. Takizawa, and T. Kuwabara, *Steel Res. Int.* 81, 1376 (2010).
- Y. Hou, J. Min, J. Lin, J.E. Carsley, and T.B. Stoughton, Cruciform specimen design for large plastic strain during biaxial tensile testing. Paper presented at the NUMISHEET 2018: 11th International Conference and Workshop on Numerical Simulation of 3D Sheet Metal Forming Processes, Tokyo, Japan, 30 July-3 Aug 2018.
- 38. A. Creuziger, M.A. Iadicola, T. Foecke, E. Rust, and D. Banerjee, JOM 69, 902 (2017).
- E.M. Mamros, S.M. Mayer, D.K. Banerjee, M.A. Iadicola, B.L. Kinsey, and J. Ha, *Int. J. Mech. Sci.* 234, 107663 (2022).

- A.H. Siddiqui, J.P. Patil, and S. Mishra, Exp. Mech. 63, 853 (2023).
- A. Ishiwatari, S. Sumikawa, J. Hiramoto, Y. Kitani, and T. Kuwabara, Enlargement of measurable strain range in biaxial cruciform test. Paper presented at the 19th International ESAFORM Conference on Material Forming, Nantes, France, 27–29 April 2016.
- J. Ha, M. Baral, and Y.P. Korkolis, J. Mech. Phys. Solids 132, 103685 (2019).
- K. Zhao, L. Chen, R. Xiao, Z. Ding, and L. Zhou, J. Mater. Sci. 54, 7231 (2019).
- 44. J. Chen, J. Zhang, and H. Zhao, Materials 15, 5001 (2022).
- S. Gerke, S. Koirala, and M. Brünig, New biaxial specimens and experiments to characterize sheet metal anisotropy and damage. Paper presented at the 19th International Conference on Experimental Mechanics, Kraków, Poland, 17–21 July 2022.
- S. Gerke, P. Adulyasak, and M. Brünig, Int. J. Solids Struct. 110–111, 209 (2017).
- M. Brünig, S. Gerke, and M. Schmidt, Int. J. Fract. 200, 63 (2016).
- M. Kim, J. Ha, S. Bonica, and Y.P. Korkolis, Double interpolation to achieve linear strain path for aisi 1008 steel cruciform specimen. Paper presented at the ASME 2022 17th International Manufacturing Science and Engineering Conference, Virtual Event, 27 June-1 July 2021.
- D.M. Collins, M. Mostafavi, R.I. Todd, T. Connolley, and A.J. Wilkinson, *Acta Mater.* 90, 46 (2015).
- S. Van Petegem, J. Wagner, T. Panzner, M.V. Upadhyay, T.T.T. Trang, and H. Van Swygenhoven, *Acta Mater*. 105, 404 (2016)
- J. Hoffman, J. Ha, B. Kinsey, D. Banerjee, and M.A. Iadicola, Double interpolation to achieve linear strain path for aisi 1008 steel cruciform specimen. Paper presented at the ASME 2022 17th International Manufacturing Science and Engineering Conference, MSEC, West Lafayette, Indiana, USA, 27 June–1 July 2022.
- A. Hannon and P. Tiernan, J. Mater. Process. Technol. 198, 1 (2008).
- A. Corti, T. Shameen, S. Sharma, A. De Paolis, and L. Cardoso, *HardwareX* 12, e00333 (2022).
- 54. T. Kuwabara, M. Kuroda, V. Tvergaard, and K. Nomura, *Acta Mater.* 48, 2071 (2000).
- Dassault Systèmes Simulia Corp, ABAQUS (Dassault Systèmes Simulia Corp, Providence, RI, USA, 2022).

**Publisher's Note** Springer Nature remains neutral with regard to jurisdictional claims in published maps and institutional affiliations.

Springer Nature or its licensor (e.g. a society or other partner) holds exclusive rights to this article under a publishing agreement with the author(s) or other rightsholder(s); author self-archiving of the accepted manuscript version of this article is solely governed by the terms of such publishing agreement and applicable law.